Published in "Journal of Power Sources 342: 231–240, 2017"
which should be cited to refer to this work.

Nanoparticle shapes of $LiMnPO_4$, Li^+ diffusion orientation and diffusion coefficients for high volumetric energy Li^+ ion cathodes

Nam Hee Kwon [a, *], Hui Yin [a], Tatiana Vavrova [a], Jonathan H-W. Lim [b], Ullrich Steiner [c], Bernard Grobéty [d], Katharina M. Fromm [a]

[a] University of Fribourg, Department of Chemistry, Chemin du Musée 9, CH-1700 Fribourg, Switzerland
[b] Cavendish Laboratory, Department of Physics, University of Cambridge, J.J. Thomson Avenue, Cambridge CB3 0HE, United Kingdom
[c] Adolphe Merkle Institute - Soft Matter Physics Group, Chemin des Verdiers 4, CH-1700 Fribourg, Switzerland
[d] University of Fribourg, Department of Geosciences, Chemin du Musée 6, CH-1700 Fribourg, Switzerland

HIGHLIGHTS

- Rod-shaped, elongated and cubic nanoparticles of $LiMnPO_4$ were synthesized.
- The shape of $LiMnPO_4$ altered the 1D diffusion direction of Li^+.
- Particles with the shortest dimension along the *b*-axis possessed the highest D_{Li+}.
- The shape of $LiMnPO_4$ affected its tap density.
- The volumetric capacity of $LiMnPO_4$ increased via the formation of dense composite.

GRAPHICAL ABSTRACT

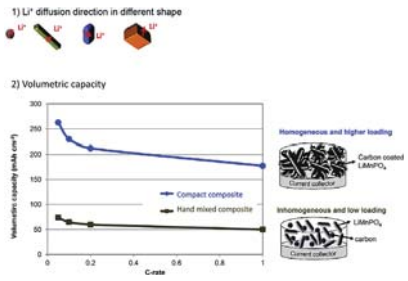

Nanoparticles of $LiMnPO_4$ were fabricated in rod, elongated as well as cubic shapes. The 1D Li^+ preferred diffusion direction for each shape was determined via electron diffraction spot patterns. The shape of nano-$LiMnPO_4$ varied the diffusion coefficient of Li^+ because the Li^+ diffusion direction and the path length were different. The particles with the shortest dimension along the *b*-axis provided the highest diffusion coefficient, resulting in the highest gravimetric capacity of 135, 100 and 60 mAh g^{-1} at 0.05C, 1C and 10C, respectively. Using ball-milling, a higher loading of nano-$LiMnPO_4$ in the electrode was achieved, increasing the volumetric capacity to 263 mAh cm^{-3}, which is ca. 3.5 times higher than the one obtained by hand-mixing of electrode materials. Thus, the electrochemical performance is governed by both the diffusion coefficient of Li^+, which is dependent on the shape of $LiMnPO_4$ nanoparticles and the secondary composite structure.

1. Introduction

Energy storage systems are necessary when the electrical energy is produced excessively from renewable energy devices and to provide energy whenever needed. One of the promising methods to store energy is by using electrochemically rechargeable system such as Li-ion batteries.

Olivine structured materials, $LiMPO_4$ (M = Fe, Mn, Co, Ni) are well known to possess an excellent structural stability versus Li^+

* Corresponding author.
E-mail address: namhee.kwon@unifr.ch (N.H. Kwon).

insertion/extraction. The covalent P-O bond strengthens the framework such that it does not collapse upon redox processes occurring at the transition metal ion $M^{2+/3+}$ [1]. This structural property of olivines provides the outstanding cyclability and thermal stability in the application of lithium ion batteries [2–6].

Among olivine materials, $LiFePO_4$ has been commercialized due to its facile synthesis and its higher electronic conductivity compared to other olivine materials. The drawback of $LiFePO_4$ is a low potential (3.6 V vs. Li^+/Li), leading to a maximum energy density of 578 Wh kg^{-1} (170 mAh g^{-1} × 3.6 V). In contrast, $LiMnPO_4$ has a higher potential (4.1 V vs. Li^+/Li) with 171 mAh g^{-1} theoretical capacity, thus providing a potentially 20% higher energy density of 701 Wh kg^{-1} (170 mAh g^{-1} × 4.1 V) than that of $LiFePO_4$. $LiCoPO_4$ and $LiNiPO_4$ have even higher cell potentials of 4.8 and 5.1 vs. Li^+/Li, respectively, but a lack of stable electrolytes at such high potentials, preventing their commercial application [7–9]. Thus, $LiMnPO_4$ is a strong candidate as cathode material for high energy Li-ion batteries.

To be used in a battery, $LiMnPO_4$ is also required to have good rate capabilities such as > 70% of theoretical capacity at 1C. A two-pronged approach in reducing the particle size of $LiMnPO_4$ on one hand and having a carbon coating on the surface of $LiMnPO_4$ particles on the other hand are most promising ways to obtain the high capacity due to the improvement of both ionic and electronic conductivity. Recently, Hatta et al. reported a high rate capability using pyrolytic carbon and Li_3PO_4 coating on rod shaped $LiMnPO_4$ nanoparticles, providing 160 and 145 mAh g^{-1} at 0.1C and 1C, respectively [10]. Platelet shaped $LiMnPO_4$ was reported to have a discharge capacity of 100 and 113 mAh g^{-1} at 1C at room temperature and 50 °C, respectively [4].

Furthermore, the Li^+ diffusion has to be controlled in the olivine materials. Olivines typically consist of slightly distorted LiO_6 and MO_6 octahedra and PO_4 tetrahedra in the crystal structure [1,11,12]. For $LiMnPO_4$ with space group *Pnma*, the Li^+ ion diffusion occurs in a zigzag-ed path along the *b* axis via edge sharing LiO_6 octahedra [13,14]. One way to improve the rate capability is thus to shorten the [010] diffusion path for Li^+ ion release and insertion. In addition, the exposure of the (010) facet on the surface of $LiMnPO_4$ particles can accelerate the kinetics of Li^+ in the *Pnma* system [15–17]. Controlling the morphology and crystal size is thus vital for the battery performance as these parameters determine the preferred direction of the Li^+ diffusion channel and the shape of the particles [18,19].

To control the morphology and surface structure of $LiMnPO_4$ particles, synthetic parameters such as precursors, surfactants and solvents play an important role [4,20–24]. Obtaining $LiMnPO_4$ nanoparticles is however more difficult than for $LiFePO_4$. When the same synthesis method is applied to generate both, the particle size of $LiFePO_4$ is smaller than the one of $LiMnPO_4$ [25]. Various synthesis routes have so far produced morphologies of $LiMnPO_4$ with spherical [26], plate-shaped [4,27,28], rods [25,29,30], wires [31,32], microporous [33] and flower-like structures [34,35]. Their electrochemical properties were affected by different morphologies of $LiMnPO_4$ [36], which may have different orientations of Li^+ diffusion.

While one advantage of using nanoparticles is to improve rate capabilities [2,4,23,37–39], however, as their surface area is higher than the one of micron-sized particles, the volume of a nanomaterial composite is extremely high due to the empty space between the particles, resulting in a low tap density. This feature decreases the loading of nanomaterial on the specific area of the current collector and limits the volumetric energy density of nanomaterials based batteries. In case of $LiFePO_4$, the formation of micron-sized secondary particles increases the volumetric energy density compared to nanoparticles, increasing thus the tap density of the composite. Liu et al. increased the tap densities of $LiMn_{0.4}Fe_{0.6}PO_4$ and carbon by the formation of a secondary microsphere composite prepared by spray drying [26]. For a micron-sized composite consisting of nano-$LiFePO_4$ and carbon, the volumetric discharge capacity increased was shown to increase by a factor of 2.5 compared to the one of nano-$LiFePO_4$ alone [40].

Therefore, there are a few challenges remaining for $LiMnPO_4$; 1) generating a desired shape of nano-$LiMnPO_4$ in a controlled way in order to facilitate Li^+ mobility, 2) improving the volumetric energy density of $LiMnPO_4$ nanomaterial without losing the high performance property of $LiMnPO_4$ and 3) optimising the specific capacity of this nano-$LiMnPO_4$, which is still a challenge probably due to the inhomogeneous mixing between agglomerated nanoparticles of $LiMnPO_4$ and carbon [35].

Although the particle shapes of $LiMnPO_4$ and their electrochemical performances were reported, Li^+ diffusion coefficients combined with the diffusion orientations were not further investigated in different shapes of particles. We present here a synthesis method based on thermal decomposition which allows us to obtain various sizes and shapes of $LiMnPO_4$ nanoparticles. The direction of the ionic diffusion (*b*-axis) in particles of various shapes was investigated using TEM electron diffraction in combination with the Li^+ diffusion coefficients ($\tilde{D}_{Li}$) on single particles. We furthermore examined the tap densities of various morphologies of nano-$LiMnPO_4$ and its composites with carbon. The volumetric and gravimetric capacities were further investigated with those materials.

2. Experimental

2.1. Chemicals

Manganese nitrate hexahydrate ($Mn(NO_3)_2 \cdot 6H_2O$), manganese acetate tetrahydrate ($Mn(CH_3COO)_2 \cdot 4H_2O$, >99%), manganese chloride tetrahydrate ($MnCl_2 \cdot 4H_2O$, >98%), lithium hydroxide monohydrate ($LiOH \cdot H_2O$, >98%), oleic acid ($C_8H_{15}COOH$, >99%), oleylamine ($C_9H_{17}NH_2$, >70%), citric acid ($C_6H_8O_7$, >99%) and solvents (benzyl ether, ethanol, hexane and *N*-methyl-2-pyrrolidone) were purchased from Sigma-Aldrich and Acros and used as received. Ketjenblack carbon, polyvinylidene fluoride (PVDF, $-(C_2H_2F_2)_n-$) and separators were supplied by Akzo Noble, Arkema Inc. in Philadelphia and Celgard in North Carolina, respectively.

2.2. Synthesis of $LiMnPO_4$

$LiMnPO_4$ material was prepared by the thermal decomposition method using oleic acid and oleylamine as surfactants and reducing agents. The detail experiments are described in our previous study [30]. To obtain the different shapes of nano-$LiMnPO_4$, 3 mmol of each manganese precursor ($Mn(NO_3)_2 \cdot 6H_2O$, $Mn(CH_3COO)_2 \cdot 4H_2O$ or $MnCl_2 \cdot 4H_2O$) and $LiOH \cdot H_2O$ were dissolved in 9 or 27 mmol oleic acid ($C_8H_{15}COOH$) during heating until 120 °C. 20 ml of benzyl ether was added to the solution afterwards with continuous heating. 9 or 27 mmol oleylamine ($C_9H_{17}NH_2$) and 3 mmol H_3PO_4 were injected at 230 °C of the solution. The solution was stirred vigorously and kept at 230 °C for 1.5 h. Then the temperature was increased to between 265 and 280 °C for 1–4 h. After the reaction, the suspension was centrifuged to collect the sedimented dark brown powder. This material is rinsed with ethanol and hexane and then centrifuged.

A ligand-exchange method using citric acid aqueous solution was applied in order to remove the organic residue in as-synthesized $LiMnPO_4$ after rinsing [30]. The organic residue containing dark brown $LiMnPO_4$ powder turned to greyish white after the ligand-exchange.

2.3. Characterization

As-synthesized $LiMnPO_4$ materials have been characterized by various methods. X-ray diffraction using Cu-radiation (Rigaku) was employed to identify the phase and to determine the crystallite sizes. XRD data were collected from 2 theta = 13 to 70° at a scan rate of 0.02° per step and 6 s per point. The crystallite size of $LiMnPO_4$ was determined by two methods; 1) Rietveld refinement and 2) the Scherrer equation ($d = K\lambda/(B\cos\theta)$, where d is the mean crystallite size in volume-weight, λ is the wavelength of the X-rays, B is the width of a peak at a half maximum due to size effects assuming that there is no strain, K is a constant value of 0.89, and θ is the incident angle). Rietveld refinement was performed with X'pert HighScore Plus software using pseudo-Voigt profile. To obtain the best refinement fitting, the reliability factors, R_{wp} (weighted profile R factor) and R_{exp} (expected R-factor) of Rietveld refinement were between 2 and 5%. Brunauer- Emmett - Teller (BET) nitrogen absorption method was applied to measure the specific surface area using Micromeritics, ASAP 2010. Thermogravimetric analysis (TGA) was used for thermal analysis under air until 800 °C at 10 °C/min. The morphology and the size of particles were studied by scanning electron microscopy (SEM, Philips XL30, 10–15 kV) and transmission electron microscopy (TEM, FEI/Philips CM-100, 80 kV). Electron diffraction spot patterns of various shaped $LiMnPO_4$ particles were obtained to determine *b*-axis of lithium ion diffusion path in *Pnma* space group. Fourier transform infrared (FT-IR) spectroscopy was employed for the surface analysis. The IR spectra were collected in the range of 600–4000 cm^{-1} using attenuated total reflectance method.

2.4. Composites of $LiMnPO_4$ and carbon

$LiMnPO_4$ was mixed with 20 wt% of carbon black using a ball mill (RETSCH) for 60 min or without ball milling. Ball milling was carried out in a 5 ml of stainless steel jar with 30 pieces of stainless steel balls of 3 mm in diameter.

2.5. Tap density

To determine the tap densities of $LiMnPO_4$ nanoparticles, microparticles and the composite of C-$LiMnPO_4$, 0.5 g of powder is inserted in a cylinder and taped for 30 times, keeping a constant tapping height then measured the volume.

2.6. Electrodes

The carbon contained $LiMnPO_4$ composite (C-$LiMnPO_4$) was mixed with polyvinylidene fluoride (PVDF) binder and carbon black in *N*-methyl-2-pyrrolidone (NMP). The weight ratio of active material $LiMnPO_4$, carbon and the binder was 67:26.3:6.7. The slurry was deposited on Al current collector using the doctor-blade method. The electrodes were dried at 120 °C under vacuum overnight. The loading of active material in the electrode was varied between 0.5 and 6 mg cm^{-2} to study the volumetric capacities.

2.7. Electrochemical properties

The electrode was assembled with lithium metal as a counter electrode, ethyl carbonate (EC) and dimethyl carbonate (DMC) mixture in 1:1 vol ratio with 1 M $LiPF_6$ electrolyte and a Celgard separator in a coin cell in an Ar filled glove box (MBraun, Germany). To evaluate charge/discharge behaviours, the assembled coin cells were tested using an Arbin 2000 battery test instrument. The measurements were carried out at a constant current and constant voltage (CCCV) or a constant current (CC) mode during charging between 2.5 and 4.6 V vs Li^+/Li. The current densities were varied between C/20 and 10C with the theoretical capacity of 171 mAh/g. To evaluate Li ion diffusion coefficients, cyclic voltammetry and electrochemical potential spectroscopy (EPS) were applied to a three-electrode cell in an Ar filled glove box using lithium anode and reference electrodes with 1 M $LiPF_6$ EC/DMC electrolyte. The measurement conditions of cyclic voltammetry were 1, 0.7, 0.5, 0.2 and 0.1 mV/s of sweep rate between 3.5 and 4.5 V vs Li^+/Li of the voltage window. The measurement conditions of EPS is described in the supplementary information.

3. Results

3.1. Controlling size and shape of $LiMnPO_4$ nanoparticles

The thermal decomposition method was used to synthesize different shapes and sizes of $LiMnPO_4$ nanoparticles. We found that the concentration of oleic acid plays a crucial role for the general particle shape, while the reaction temperature influences the thickness and the length of the particles, and hence their aspect ratio. We also studied the influence of different kinds of precursors and their concentrations. Manganese acetate ($Mn(CH_3COO)_2{\cdot}4H_2O$) formed polyhedral nanoparticles with a mean diameter of 34 nm (Fig. S1(a)) after 1 h. Upon reaction times greater than 1.5 h, the polyhedral particles of $LiMnPO_4$ grew preferentially in one direction to yield slightly elongated spherical particles (Fig. 1a and b). Using a three times higher concentration of precursor than for Fig. 1a and b increases the particle size and leads to rod-shaped particles with rounded corners (Fig. 1c and d). With manganese chloride as precursor under similar concentration conditions as for particles shown in Fig. 1a and b, $LiMnPO_4$ forms thinner and longer rod-shaped particles (Fig. 1e and f). The specific surface area of $LiMnPO_4$ using manganese chloride (26.8 $m^2\ g^{-1}$, Fig. 1e and f) is almost half compared to the one using manganese acetate (51 $m^2\ g^{-1}$, Fig. S1. Three times higher concentrations of $MnCl_2$ leads to thicker and rather cubic/platelet shapes (Fig. 1g and h). In a previous study by us, manganese nitrate as precursor provided needle, rod and spherical shapes [30].

The precursors and their concentration thus strongly affect the particle shape and size.

Oleic acid and oleylamine prevent the further growth into micron-sized particles and also their agglomeration in solution. Indeed, their hydrophilic OH-anchors rather bind to metal ions while their hydrophobic hydrocarbon moieties point into the non-polar solvent benzyl ether.

After the reaction with the surfactants in benzyl ether, the colour of the so-obtained $LiMnPO_4$ material is typically dark brown, indicating the presence of residual surfactants. We therefore used our ligand exchange method efficiently to remove the surfactants from the surface and to yield "clean" light grey $LiMnPO_4$ nanoparticles without organic residues [30].

Table 1 shows the summary of $LiMnPO_4$ characteristics in terms of the shapes, specific surface areas, mean particle sizes and crystallite sizes. The crystallite sizes were determined using the Scherrer equation ($d = K\lambda/(B\cos\theta)$, d is the mean size of the crystalline domains, K is the shape factor, λ is the X-ray wavelength, B is the line broadening at half the maximum intensity and θ is the incident angle) and Rietveld refinement. The reliability factors, R_{wp} (weighted profile R factor) and R_{exp} (expected R-factor) of Rietveld refinement were between 2 and 5% (Fig. S2). The crystallite sizes determined by Rietveld refinement showed smaller than the ones by Scherrer equation. In Rietveld refinement, all peaks of XRD patterns were fitted using pseudo-Voigt function and Lorentzian coefficient of peak shape factor while in Scherrer equation, one specific peak of $2\theta = 20.6°$ was applied. As you see in the table, the

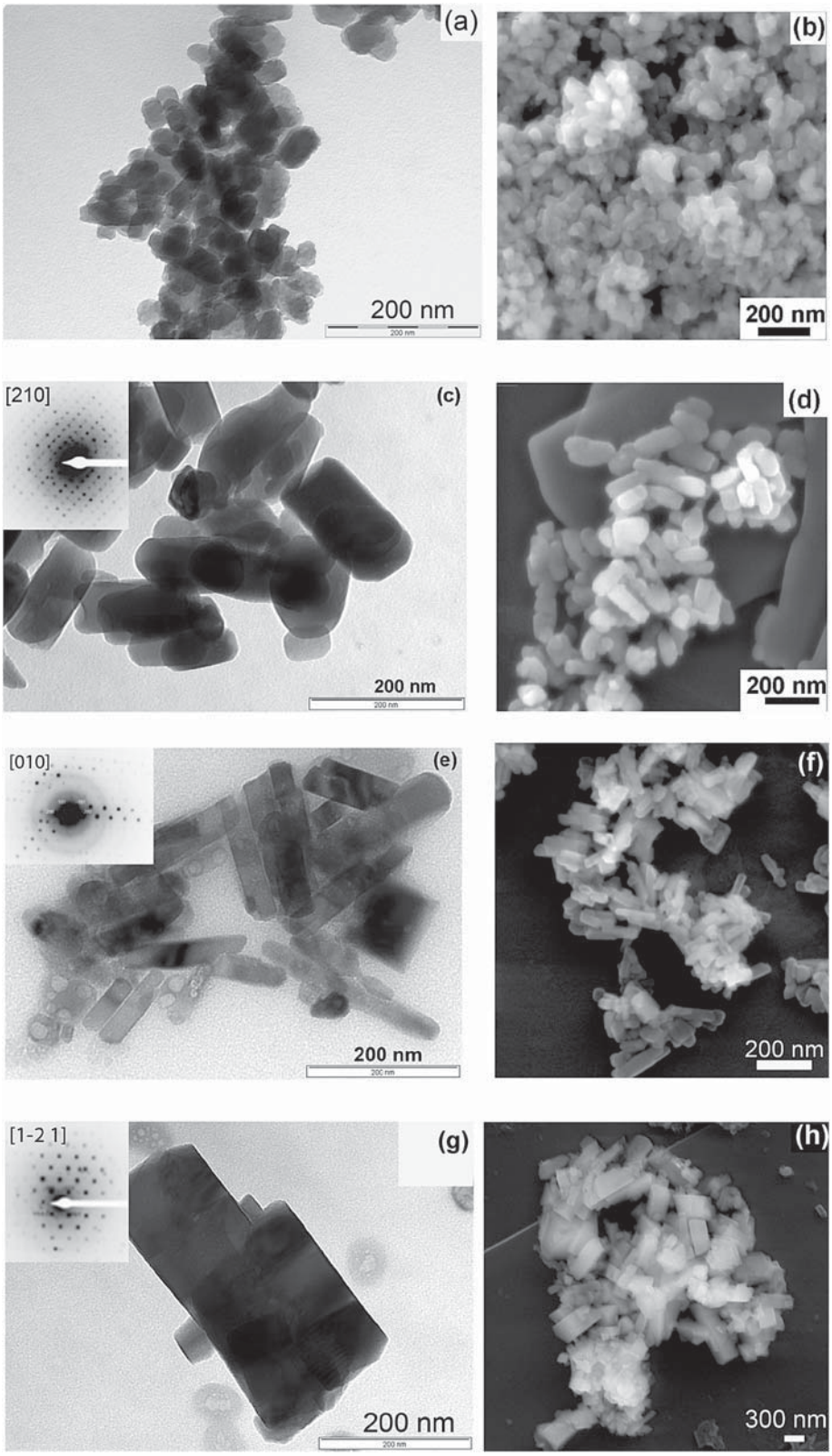

Fig. 1. TEM (left) and SEM (right) pictures of $LiMnPO_4$ with different morphology controlled by different manganese precursors and the concentration of the precursors. TEM: (a) and (c) are from $Mn(CH_3COO)_2{\cdot}4H_2O$ using 3 and 9 mmol of manganese precursors, respectively. (e) and (g) are from $MnCl_2{\cdot}4H_2O$ precursor with 3 and 9 mmol, respectively. The SEM images on the right correspond to the material shown on the left. The insets are electron diffraction spot patterns.

material having higher specific surface area provided smaller crystallite size in both Scherrer equation and Rietveld refinement methods.

3.2. Tap densities of $LiMnPO_4$ and its composites

In general, nanoparticles have low tap density due to their high

Table 1
The summary of characteristics of variously shaped and sized $LiMnPO_4$.

Shape of particles	Size by TEM (nm)	Size of crystallite (nm)[a]	S_{BET} ($m^2\ g^{-1}$)	Particle size by S_{BET} (nm)[b]	Precursors
Polyhedral		21 (20)	51.38	34	$Mn(CH_3COO)_2{\cdot}4H_2O$
Elongated sphere		32 (26)	35.07	49	$Mn(CH_3COO)_2{\cdot}4H_2O$
Thick rod		52 (34)	28	62	$Mn(CH_3COO)_2{\cdot}4H_2O$
Thin rod	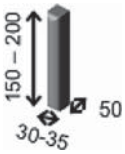	34 (28)	26.8	65	$MnCl_2{\cdot}4H_2O$
Cubic/plate	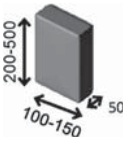	59	14.2	122	$MnCl_2{\cdot}4H_2O$
Needle [30]		20 (16)	67	26	$Mn(NO_3)_2{\cdot}6H_2O$

[a] Crystallite sizes by Rietveld refinement method with the one from the Scherrer equation in parenthesis.
[b] The particle size d is calculated by the equation of $d = K/(\rho \times S_{BET})$, where K is the shape factor, ρ is the density of the material and S_{BET} is the specific surface area of the material.

surface area, causing poor loading of active material in the electrode. The tap density is a useful indication to estimate particle packing that can be varied with the surface area of the materials and the shape of particles [41,42]. We investigated the tap densities of elongated spherical, rod, cubic and needle shaped nano-$LiMnPO_4$ as well as micron sized $LiMnPO_4$ particles, all shown in Table 2. It is not surprising that micron sized $LiMnPO_4$ has 1.79 g ml^{-1} of tap density while all nano-sized $LiMnPO_4$ particles reach between 1 and 0.5 g ml^{-1}. The powder packing density is different depending on the shape of nanoparticle as shown in the schematic of Fig. 2. The needle shaped $LiMnPO_4$ had the lowest tap density of 0.54 g ml^{-1} due to the high aspect ratio while the elongated spherical particles of $LiMnPO_4$ had the highest tap density of 1.07 g ml^{-1}. Thus, the shapes of nano-$LiMnPO_4$ affected their tap densities. This can be explained by the rationale that spherical particles have the highest number of contact points (six contacts per sphere), which allows for the highest packing density among the various shaped particles. The tap density decreases as the particle shape deviates more and more from the sphere [42]. Experimental studies indeed showed that the tap density of spheres has the highest value while the needle-shaped particles had the lowest tap density among cylinder, cube and needle-shaped particles [43,44].

The tap densities of the composites formed from nano-rod $LiMnPO_4$ and high surface area carbon (ketjenblack) have been investigated. The composites were prepared either by hand-mixing or ball-milling. When the nano-rod $LiMnPO_4$ particles are hand-mixed with the carbon, the tap density (0.27 g ml^{-1}) of this composite is relatively low. However, after the ball-milling of the composite, the tap density increased to 0.77 g ml^{-1}, almost 3 times higher than the one prepared by hand-mixing. During the ball-milling, nanoparticles of $LiMnPO_4$ and carbon make an intimate

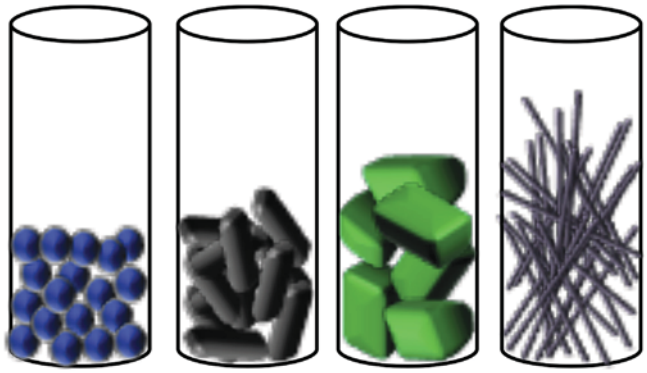

Fig. 2. The schematic of powder packing densities containing different shapes of nanoparticles.

Table 2
The tap densities of micron-sized $LiMnPO_4$, nano-sized $LiMnPO_4$ with different shapes and the composites of nano-$LiMnPO_4$ and carbon.

	Micro-$LiMnPO_4$	Nano-$LiMnPO_4$				Composite	
		Elongated	Thin rod	Plate/Cubic	Needle	Mixed	Compact
Tap density (g ml^{-1})	1.79	1.07	0.97	0.77	0.54	0.27	0.77
SSA ($m^2\ g^{-1}$)	0.92	30.2	26.8	14.2	67	30	6.26

contact and form dense agglomerates (Fig. 3). Hence, the dense agglomerations via ball-milling increased the tap density and a loading of active material. Consequently, the specific surface area decreased from 30 $m^2\ g^{-1}$ of hand mixed material to 6.26 $m^2\ g^{-1}$ after the ball-milling. The mean pore size is also reduced from 40 nm for hand mixing to 15 nm after ball milling (Fig. S3). We assume that this is similar to the reported micron-sized secondary composite agglomeration which improves the tap density of $LiFe_{0.6}Mn_{0.4}PO_4/C$ and $LiFePO_4/C$, resulting in higher volumetric capacities of $LiFe_{0.6}Mn_{0.4}PO_4$ and $LiFePO_4$ [26,40,45].

3.3. Li^+ diffusion coefficients and diffusion direction

The D_{Li}^{+} of the different materials was determined using cyclic voltammetry on electrodes consisting of the different shapes of $LiMnPO_4$. Fig. 4 shows an example of typical redox curves at various scan rates for one of the particle types. The cathodic current peaks were determined at each scan rate and used for a graph as a function of square root of scan rate shown in the inset Fig. 4. The slope of the inset graph is then D_{Li}^{+} according to the Randles-Sevcik equation.

$$I_p = (2.69 \times 10^5)\, n^{3/2} A\, D_{Li}^{1/2}\, C\, v^{1/2}$$

where I_p is the current peak, n is the number of electrons, A is the surface area of the electrode, D is the diffusion coefficient, C is the concentration of Li^+ and v is the scan rate.

Table 3 summarizes the values of D_{Li}^{+} as a function of the shape of $LiMnPO_4$, the surface areas and their mean particle sizes. Interestingly, the electrodes consisting of thick and thin rod-shaped $LiMnPO_4$ particles have almost the same specific surface areas, 28 and 26.8 $m^2\ g^{-1}$ respectively, but as far as the D_{Li}^{+} is concerned, there is one order of magnitude difference between those materials. We attribute this to the influences of size and shape of $LiMnPO_4$ particles and the orientation of the *b*-axis on the lithium ion diffusion. Indeed, the thick rod $LiMnPO_4$ particles have a Li^+ diffusion length of 60 nm in a single particle along the *b*-axis while the thin and long rod $LiMnPO_4$ particles have the shorter diffusion length of 30–35 nm in a single particle. If the lithium ion diffusion would occur along the longest length in both rod shapes of $LiMnPO_4$, the thin rod shaped $LiMnPO_4$ should have a lower diffusion coefficient as they are longer with 150–200 nm than the thick rods with 100–150 nm. However, our measurement revealed that the diffusion coefficient of Li^+ in the electrode with thin rods $LiMnPO_4$ is almost 10 times higher than the one for thick rods. This

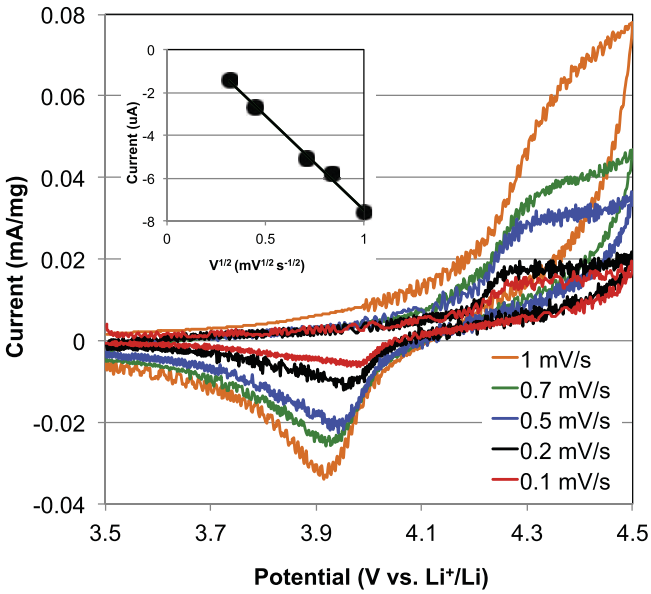

Fig. 4. The cyclic voltammograms of one of the $LiMnPO_4$ electrodes at various scan rates. The inset graph is the cathodic current peak as a function of square root of each scan rate.

means that the Li^+ diffusion occurs along the shortest dimension of the single particles. Afterwards, the direction of Li^+ diffusion in a single particle was determined by electron diffraction spot patterns shown in the insets of Fig. 1 (c), (e) and (g). It showed that the b-axis where lithium ion is diffused in the structure is the shortest dimension in all different shaped $LiMnPO_4$ particles. Thus, both analyses agree well each other. Another confirmation comes from the D_{Li}^{+} of $1.6 \pm 1.1 \times 10^{-11}$ $cm^2\ s^{-1}$ for elongated spherical $LiMnPO_4$ particles with 34 nm of mean particle diameter. This value is very close to the D_{Li}^{+} value of thin rod $LiMnPO_4$, $2 \pm 1.1 \times 10^{-11}$ $cm^2\ s^{-1}$ although the specific surface area of the elongated spheres (51.4 $m^2\ g^{-1}$) is twice the one of thin rods (26.8 $m^2\ g^{-1}$). It proves again that the Li^+ diffusion direction occurs along the short dimension (30–35 nm) of the thin rods. Also, thick rod and cubic $LiMnPO_4$ have similar D_{Li}^{+} values due to the similar Li^+ diffusion path length of 60 nm although the specific surface area of thick rod is twice (28 $m^2\ g^{-1}$) the one of cubic particles (14.2 $m^2\ g^{-1}$). Therefore, we could determine the direction of lithium ion diffusion which is the shortest dimension in a single particle by

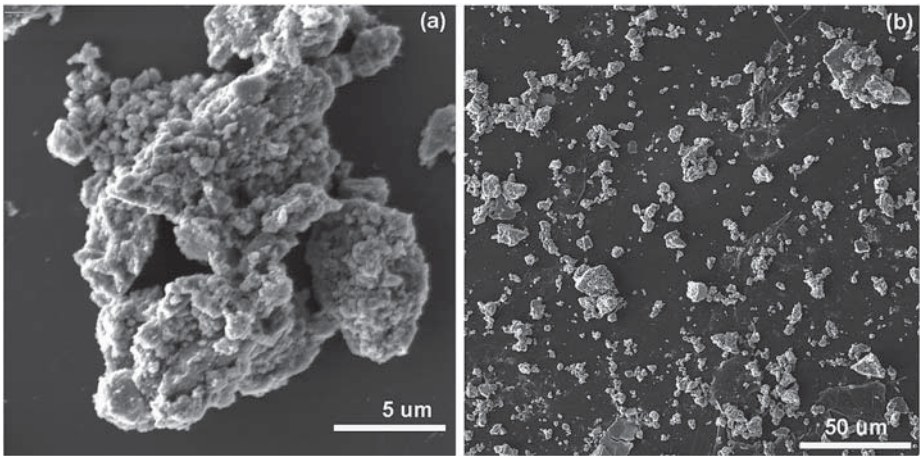

Fig. 3. SEM images of the composite of nano-$LiMnPO_4$ and carbon.

Table 3
The summary of D_{Li}^{+} with different shapes of $LiMnPO_4$ nanoparticles, their specific surface areas, the mean particle sizes and the estimated Li^+ diffusion orientation.

$LiMnPO_4$ particle			D_{Li}^{+} ($cm^2\ s^{-1}$)	Li^+ diffusion direction
Shape	Surface area ($m^2\ g^{-1}$)	size (nm)		
Elongated sphere	51.4	34	$1.6 \pm 1.1 \times 10^{-11}$	
Thick rod	28.0	62	$1.3 \pm 5.6 \times 10^{-12}$	
Thin rod	26.8	65	$2.0 \pm 1.1 \times 10^{-11}$	
Cubic	14.2	122	$9.2 \pm 3.9 \times 10^{-12}$	

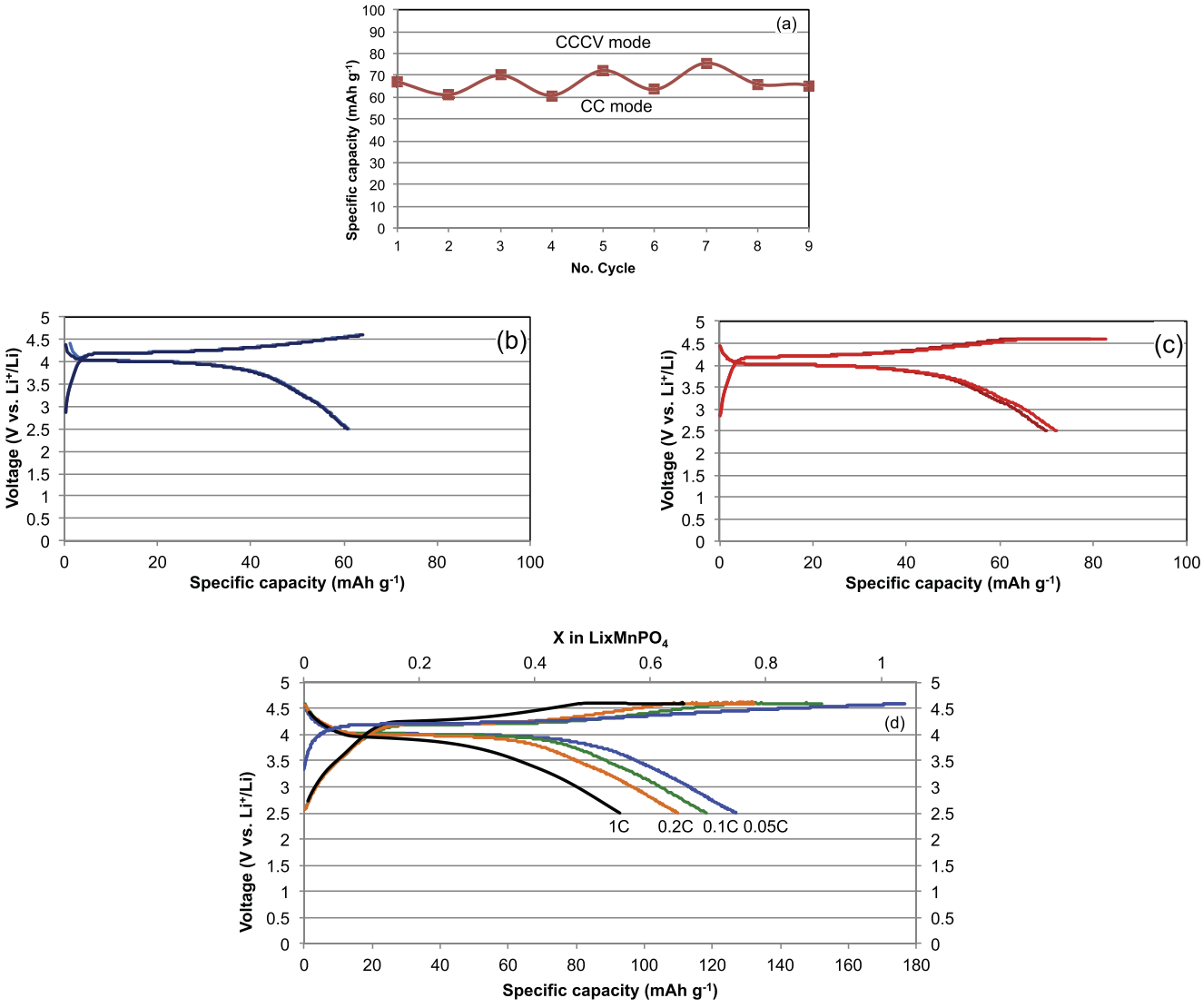

Fig. 5. (a) The discharge capacities at CC and CCCV mode in terms of cycle. (b) and (c) The charge and discharge curves of elongated spherical shaped $LiMnPO_4$ electrodes in CC and CCCV modes at 0.1 C, respectively. (d) The charge and discharge curves of thin rod $LiMnPO_4$ particles at various C-rates.

combined analysis of D_{Li}, morphology and electron diffraction spot pattern.

We evaluated D_{Li}^{+} of the electrodes by another electrochemical technique of electrochemical potential spectroscopy (EPS) described in supplementary information. The electrode consisting of elongated spherical $LiMnPO_4$ had D_{Li}^{+} of $3.4 \pm 1.2 \times 10^{-11}\ cm^2\ s^{-1}$

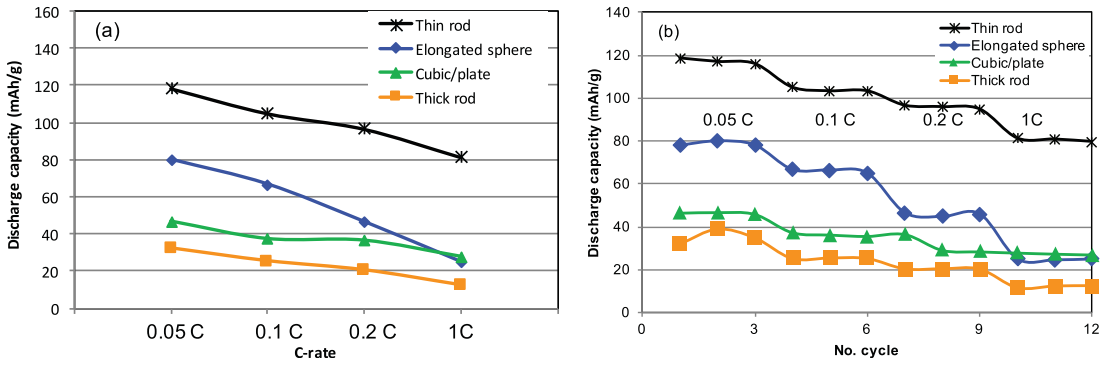

Fig. 6. (a) The rate capabilities of $LiMnPO_4$ cathodes consisting of different shapes of nanoparticles. (b) The cyclability of $LiMnPO_4$ cathodes at various current densities.

when Li^+ insertion and extraction occur. This is very close to the value determined by cyclic voltammetry method. The other electrode of thin rod $LiMnPO_4$ obtained $3.8 \pm 3.1 \times 10^{-10}$ cm^2 s^{-1}. Thus, the trend of D_{Li}^{+} determined by EPS is the same as cyclic voltammetry.

3.4. Electrochemical properties

It is known that olivine structured $LiMnPO_4$ should be tested under constant current and constant voltage mode (CCCV) after reaching the desired upper potential in order to extract Li^+ fully from the structure of $LiMnPO_4$. We thus examined two different measurement modes of CC (constant current) and CCCV shown in Fig. 5. CCCV mode provided higher specific capacity because the constant voltage condition allowed more Li^+ ions to be extracted and re-inserted into the structure of $LiMnPO_4$. These reactions are reversible when we switch between CCCV and CC mode repeatedly as shown in Fig. 5a. The charge/discharge curves of the first and 5th cycles in CC are almost identical (Fig. 5b) and the behaviours are the same in CCCV (Fig. 5c). Thus, the elongated spherical shaped $LiMnPO_4$ electrodes showed high electrochemical stability. We also tested thin-rod shaped $LiMnPO_4$ electrode in CCCV mode shown in Fig. 5d. The specific capacities of this electrode increased at all the varied C-rates compared to the elongated spherical $LiMnPO_4$ electrode.

The specific capacities of $LiMnPO_4$ electrodes consisting of various shapes of $LiMnPO_4$ nanoparticles were examined at various scan rates (Fig. 6). It shows that the capacities vary with the shape of $LiMnPO_4$ nanoparticles. The highest specific capacity of 120 mAh g^{-1} was achieved using thin rod $LiMnPO_4$ nanoparticles at 0.05C. At 1C, this electrode yielded 80 mAh g^{-1}. On the other hand, the lowest specific capacity of 35 mAh g^{-1} was observed with the thick rod $LiMnPO_4$ electrode at 0.05C. The highest and lowest values of capacities agree well with the values of D_{Li}^{+}; the lowest diffusion coefficient of Li^+ provided the lowest capacity.

The rate capabilities at higher C-rates (>1C) were further investigated with thin-rod $LiMnPO_4$ electrodes as shown in Fig. 7 (a). We obtained even higher specific capacities using 3 wt % of vinylene carbonate (VC) additive in EC:DMC 1 M $LiPF_6$ electrolyte. The specific capacities were 100–95 and 60 mAh/g at 1C and 10C, respectively. Fig. 7 (b) shows the cyclabilities of thin-rod $LiMnPO_4$ electrodes at C/20 and 1C. It reached 135 mAh/g upon 50 cycles with no degradation at C/20 while it obtained 84 mAh/g at 50th cycle with 76% of retention at 1C.

The formation of dense secondary composite particles by ball-milling increased the tap density by a factor of 3 compared to the composite prepared by hand-mixing. The volumetric capacities were investigated with the compact and hand-mixed composites,

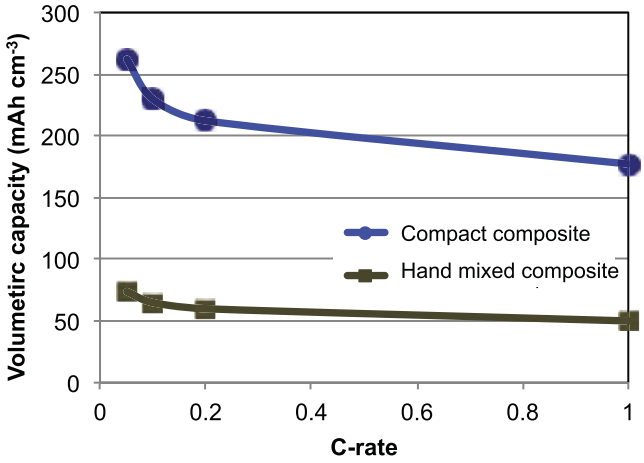

Fig. 7. (a) The rate capabilities of thin rod-shaped $LiMnPO_4$ cathodes using 3 wt % of VC additive in EC:DMC 1 M $LiPF_6$ electrolyte. (b) The cyclability of thin rod LiMnPO4 electrodes at C/20 and 1C using 3 wt % of VC additive in EC:DMC 1 M $LiPF_6$ electrolyte.

assuming that the gravimetric capacities of both electrodes are identical (Fig. 8). The dense composite $LiMnPO_4$/C electrode based on rod-shaped particles had 262 mAh cm^{-3}, 3.5 times higher volumetric capacity than the one of hand-mixed composite electrode (75 mAh cm^{-3}) because of the higher loading of active material (2.1 g cm^{-3}) compared to 0.62 g cm^{-3} of loading by hand-mixing. We are further developing an optimization to maximize both gravimetric and volumetric capacities of $LiMnPO_4$ cathode for high energy lithium ion batteries.

In summary, nanoparticles of $LiMnPO_4$ provide the great advantage of high ionic diffusion due to the short path lengths of diffusion. More precisely, we showed that depending on the shape of nanoparticles, different orientations of the preferred Li^+ diffusion channel are found. Two synthesized $LiMnPO_4$ materials have the same specific surface areas but the shape and dimensions of particle are different. Then the Li^+ diffusion occurred in the shortest length of a single particle and the diffusion coefficient of Li^+ varies according to the dimension along the *b*-axis. The electrochemical capacities revealed that the electrode having the highest diffusion coefficient of Li^+ provided the highest capacity. Therefore, one should control the shape of particles to shorten the dimension of the Li^+ diffusion channel.

However, it is not always necessary to minimize all the dimensions of particles. Reducing the size of active particles may give also negative effects on the electrochemical properties such as a side-reaction with the electrolyte and poor packing density. The poor packing density results in the low volumetric capacities and

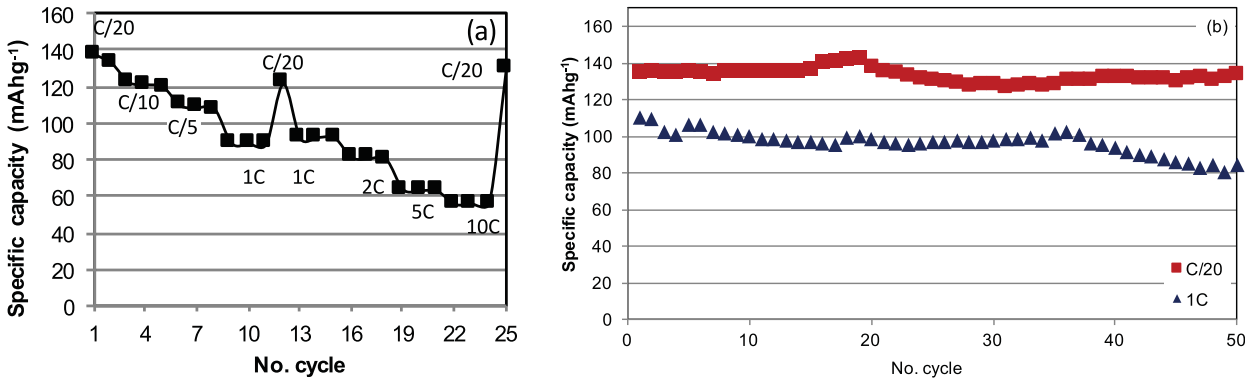

Fig. 8. The volumetric capacities of $LiMnPO_4$ electrodes prepared by ball-milling and hand-mixing of the composites, rod-shaped $LiMnPO_4$ and carbon.

energies due to its low loading of active material in the electrode.

In this report, we showed the increased volumetric capacities by the formation of secondary composite particles consisting of nano-$LiMnPO_4$ and carbon via ball milling. Therefore, we have both benefits of nanoparticles to increase the kinetic of Li^+ diffusion and significantly higher volumetric capacity by the micron sized composite dense particles.

4. Conclusion

Nanoparticles of $LiMnPO_4$ were synthesized in an elongated spherical, thin nano-rod, thick nano-rod, cubic and platelet shapes by thermal decomposition method. The shapes of $LiMnPO_4$ nanoparticles affected the tap densities, the path and the direction of Li^+ diffusion, determined by electron diffraction spot patterns and electrochemical tools. The tap density of carbon-contained composite increased 3 times higher by the formation of dense agglomeration via ball milling. The increased tap density provided the higher loading of the active material in the electrode, resulting in the higher volumetric capacity of 263 mAh cm^{-3} which is 3.5 times higher than the one of the composite prepared by hand-mixing (74 mAh cm^{-3}).

The analysis of D_{Li}^{+} revealed that the smallest particles did not have the highest Li^+ diffusion coefficient but rather the shortest dimension of the particles offered the shortest path length of Li^+ diffusion direction that gave the highest Li^+ diffusion coefficient. Thus, controlling the shortest path length of Li^+ diffusion is the critical parameter to improve the electrochemical reaction kinetics and to enhance the rate capability.

The shape of olivine particle plays a critical role to increase the loading of active nanoparticles in the electrode and to increase the capacities at high current densities. Ball milling is an effective process to make dense composite in order to increase the loading of active material in the electrode.

Acknowledgements

This work was supported by Swiss National Research Program (NRP 64; Project number 406440_141604) of 'opportunities and risks of nanomaterials', and the Swiss Competence Center for Energy Research (SCCER) Heat and Energy Storage.

Dr. Kwon leaded the project and designed the experiments and electrochemical analyses. Yin and Vavrova synthesized $LiMnPO_4$ and prepared electrodes, respectively. Jonathan H-W Lim determined Li^+ diffusion coefficients using EPS. Prof. Grobéty and Dr. Kwon did electron diffraction spot patterns and determined zone axis. Prof. Fromm supported the project of NRP 64.

Appendix. ASupplementary data

Supplementary data related to this article can be found at http://dx.doi.org/10.1016/j.jpowsour.2016.11.111.

References

[1] A.K. Padhi, K.S. Nanjundaswamy, J.B. Goodenough, J. Electrochem. Soc. 144 (1997) 1188–1194.
[2] H. Ni, J. Liu, L.-Z. Fan, Nanoscale 5 (2013) 2164–2168.
[3] J.-M. Chen, C.-H. Hsu, Y.-R. Lin, M.-H. Hsiao, G.T.-K. Fey, J. Power Sources 184 (2008) 498–502.
[4] D. Wang, H. Buqa, M. Crouzet, G. Deghenghi, T. Drezen, I. Exnar, N.-H. Kwon, J.H. Miners, L. Poletto, M. Grätzel, J. Power Sources 189 (2009) 624–628.
[5] D.D. MacNeil, Z. Lu, Z. Chen, J.R. Dahn, J. Power Sources 108 (2002) 8–14.
[6] F. Wang, J. Yang, P. Gao, Y. NuLi, J. Wang, J. Power Sources 196 (2011) 10258–10262.
[7] J. Wolfenstine, J. Allen, J. Power Sources 142 (2005) 389–390.
[8] V. Aravindan, Y.L. Cheah, W. Chui Ling, S. Madhavi, J. Electroanal. Chem. 159 (2012) A1435–A1439.
[9] K. Amine, H. Yasuda, M. Yamachi, Electrochem. Solid-State Lett. 3 (2000) 178–179.
[10] N. Hatta, Y. Yoshida, H. Tomita, J. Electrochem. Soc. 162 (2015) A1556–A1565.
[11] A. Yamada, S.C. Chung, K. Hinokuma, J. Electrochem. Soc. 148 (2001) A224–A229.
[12] A.K. Padhi, K.S. Nanjundaswamy, C. Masquelier, S. Okada, J.B. Goodenough, J. Electrochem. Soc. 144 (1997) 1609–1613.
[13] M.S. Islam, J.D. Daniel, A.J.F. Craig, R.S. Peter, Chem. Mater. 17 (2005) 5085–5092.
[14] S. Nishimura, G. Kobayashi, K. Ohoyama, R. Kanno, M. Yashima, A. Yamada, Nat. Mater. 7 (2008) 707–711.
[15] A. Whiteside, C.A. Fisher, S.C. Parker, M.S. Islam, Phys. Chem. Chem. Phys. 16 (2014) 21788–21794.
[16] B. Guo, H. Ruan, C. Zheng, H. Fei, M. Wei, Sci. Rep. 3 (2013) 2788–2793.
[17] A.J.F. Craig, M.S. Islam, J. Mater. Chem. 18 (2008) 1209–1215.
[18] D. Morgan, A. Van der Ven, G. Ceder, Electrochem. Solid State Lett. 7 (2004) A30–A32.
[19] L. Wang, F. Zhou, G. Ceder, Electrochem. Solid-State Lett. 11 (2008) A94–A96.
[20] Z. Qin, X. Zhou, Y. Xia, C. Tang, Z. Liu, J. Mater. Chem. 22 (2012) 21144–21153.
[21] K. Dokko, S. Koizumi, H. Nakano, K. Kanamura, J. Mater. Chem. 17 (2007) 4803–4810.
[22] D. Rangappa, K. Sone, M. Ichihara, T. Kudo, I. Honma, Chem. Commun. 46 (2010) 7548–7550.
[23] M. Zhao, Y. Fu, N. Xu, G. Li, M. Wu, X. Gao, J. Mater. Chem. A 2 (2014) 15070–15077.
[24] K. Dokko, T. Hachida, M. Watanabe, J. Electrochem. Soc. 158 (2011) A1275–A1281.
[25] A. Vadivel Murugan, T. Muraliganth, P.J. Ferreira, A. Manthiram, Inorg. Chem. 48 (2009) 946–952.
[26] W. Liu, P. Gao, Y. Mi, J. Chen, H. Zhou, X. Zhang, J. Mater. Chem. A 1 (2013) 2411–2417.
[27] Y. Dong, L. Wang, S. Zhang, Y. Zhao, J. Zhou, H. Xie, J. Goodenough, J. Power Sources 215 (2012) 116–121.
[28] D. Choi, D. Wang, I.T. Bae, J. Xiao, Z. Nie, W. Wang, V.V. Viswanathan, Y.J. Lee, J.G. Zhang, G.L. Graff, Z. Yang, J. Liu, Nano Lett. 10 (2010) 2799–2805.
[29] H. Wang, Y. Yang, Y. Liang, L.-F. Cui, H. Casalongue, Y. Li, G. Hong, Y. Cui, H. Dai, Angew. Chem. Int. Ed. 50 (2011) 7364–7368.
[30] N.-H. Kwon, K.M. Fromm, Electrochim. Acta 69 (2012) 38–44.
[31] Q. Lu, G.S. Hutchings, Y. Zhou, H.L. Xin, H. Zheng, F. Jiao, J. Mater. Chem. A 2 (2014) 6368–6373.

[32] Z. Pei, X. Zhang, X. Gao, J. Alloy Compd. 546 (2013) 92–94.
[33] H. Yoo, M. Jo, B.-S. Jin, H.-S. Kim, J. Cho, Adv. Energy Mater. 1 (2011) 347–351.
[34] P. Nie, L. Shen, F. Zhang, L. Chen, H. Deng, X. Zhang, CrystEngComm 14 (2012) 4284–4288.
[35] L. Bao, G. Xu, J. Wang, H. Zong, L. Li, R. Zhao, S. Zhou, G. Shen, G. Han, CrystEngComm 17 (2015) 6399–6405.
[36] J.O. Herrera, H. Camacho-Montes, L.E. Fuentes, L. Álvarez-Contreras, J. Mater. Sci. Chem. Eng. 03 (2015) 54–64.
[37] B. Kang, G. Ceder, Nature 458 (2009) 190–193.
[38] N.-H. Kwon, T. Drezen, I. Exnar, I. Teerlinck, M. Isono, M. Graetzel, Elecrochem. Solid State Lett. 9 (2006) A277–A280.
[39] D.-H. Kim, J. Kim, Elecrochem. Solid State Lett. 9 (2006) A439–A442.
[40] S.W. Oh, S.-T. Myung, H.J. Bang, C.S. Yoon, K. Amine, Y.-K. Sun, Electrochem. Solid State Lett. 12 (2009) A181–A185.
[41] A. Santomaso, P. Lazzaro, P. Canu, Chem. Eng. Sci. 58 (2003) 2857–2874.
[42] R.M.G.a.S.J. Park, Handbook of Mathematical Relations in Particulate Materials Processing, John Wiley & Sons, Inc, 2008.
[43] M.S. Hassan, R.W. Lau, AAPS PharmSciTech 10 (2009) 1252–1262.
[44] G.S. Riley, G.R. Mann, Mat. Res. Bull. 7 (1972) 163–170.
[45] D. Zane, M. Carewska, S. Scaccia, F. Cardellini, P.P. Prosini, Electrochim. Acta 49 (2004) 4259–4271.